The destructive earthquake doublet of February 6, 2023, in south-central Türkiye and northwestern Syria: initial observations and analyses

P. Martin Mai[1]*, Theodoros Aspiotis[1], Tariq Anwar Aquib[1], Eduardo Valero Cano[1], David Castro-Cruz[1], Armando Espindola-Carmona[1], Bo Li[1], Xing Li[1], Jihong Liu[1], Rémi Matrau[1], Adriano Nobile[1], Kadek Hendrawan Palgunadi[1], Matthieu Ribot[1], Laura Parisi[1], Cahli Suhendi[1], Yuxiang Tang[1], Bora Yalcin[1], Ulaş Avşar[2], Yann Klinger[3], and Sigurjón Jónsson[1]

[1] King Abdullah University of Science and Technology, Division of Physical Sciences and Engineering, 23955 Thuwal, Saudi Arabia

[2] Middle East Technical University (METU), Ankara, Türkiye

[3] Université de Paris Cité, Institut de Physique de Globe, CNRS, Paris, France

** Corresponding author*

Abstract

On February 6, 2023, two large earthquakes, magnitude 7.8 and 7.6, rocked south-central Türkiye and northwestern Syria. At the time of writing, the death toll exceeded 50,000 in Türkiye and 7,200 in Syria. The epicenter of the first mainshock was located ~15 km east of the East Anatolian Fault (EAF), the second large earthquake (9 hours later) initiated ~90 km to the north, on the east-west trending Sürgü Fault. Aftershocks delineate fault lengths of ~350 km and ~170 km, respectively. Using seismic and satellite data for first-order analyses of surface-fault offsets, space-time rupture evolution, and recorded ground-motions, our study sheds light on the reasons for the extensive destruction. The first event ruptured the EAF bilaterally, lasted for ~80 sec and created surface fault offsets of over 6 m. The second event also ruptured bilaterally, with a duration of ~35 sec and more than 7 m surface offsets. Horizontal ground accelerations reached locally up to 2g in the first mainshock; severe and wide-spread shaking occurred in the Hatay-Antakia area with values near 0.5g. Both earthquakes are characterized by directivity effects and abrupt rupture cessation generating stopping phases that contributed to strong seismic radiation. Shaking was further aggravated locally by site-amplification effects.

Introduction

The two devastating earthquakes of February 6, 2023, and their associated aftershock sequences, in south-central Türkiye and northwestern Syria are sobering reminders that earthquakes cannot be predicted, nor prevented, but only can be prepared for. The earthquakes were the deadliest ones in Türkiye for centuries. The two strong earthquakes occurred in rapid succession, but on different faults. The epicenter of the first shock of magnitude M_w 7.8 was located ~15 km east of the East Anatolian Fault (EAF) at 37.288 N, 37.043 E, 8.6 km depth, (origin time 01:17 AM UTC). Only 9:07 hours later, the second event (magnitude M_w 7.6) initiated 90 km north of the EAF on the east-west trending Sürgü Fault (38.089°N, 37.239°E, 7.0 km depth, origin time 10:24 AM UTC).

The East Anatolian Fault defines the active plate boundary between the Arabian and the Anatolian Plates (Figure 1a). Over its ~500 km length, the left-lateral EAF has an estimated slip rate of ~10 mm/yr (*Aktug et al., 2016*). Together with the right-lateral North Anatolian Fault (NAF), the EAF bounds the westward extrusion of the Anatolian Plate from the Arabia-Eurasia collision zone (*Pousse-Beltran et al, 2020, and references therein*). The section of the EAF that broke in the first mainshock extends into the Hatay triple junction between the EAF, the Cyprus arc, and the Dead Sea Fault branching to the south (Figure 1b).

During the last ~100 years, both the NAF and EAF varied in terms of releasing tectonic stress in large earthquakes. The NAF produced a sequence of large earthquakes in the 20th century that initiated with the 1912 M_w 7.2 Ganos earthquake at the western end of the Marmara Sea, and then continued with the devastating M_w 7.8 Erzincan earthquake in 1939 on the eastern NAF that killed over 30,000 people. This tragic quake was followed by 10 moderate-to-large events (1942 - 1967; *Barka, 1996*) and the 1999 M_w 7.6 Izmit and M_w 7.2 Duzce earthquakes east of the Marmara Sea, leaving major fault segments near Istanbul unbroken since 1766. In contrast, only three moderately sized earthquakes occurred on the EAF in the last ~50 years (M_w 6.7 in 1971; M_w 6.1 in 2020; M_w 6.8 in 2020), located on the northwestern section of the EAF. However, large historical earthquakes are documented along the southern EAF (*Ambraseys, 2009; Meghraoui, 2015*), such as in 1114 CE (M_w ~7.8), 1872 CE (M_w ~7.2), and 1822 CE (M_w ~7.5). The second rupture of the 2023 earthquake sequence occurred on the Sügür fault, a side branch of the EAF strand that is thought to have last ruptured in 1544 CE (Figure 1a). The seismic activity of the NAF and EAF is reflected in corresponding seismic hazard maps (e.g., *Pagani et al. 2018; Akkar et al., 2018*; *Şeşetyan et al., 2018*; *Demircioğlu et al., 2018*) (Figure 1b).

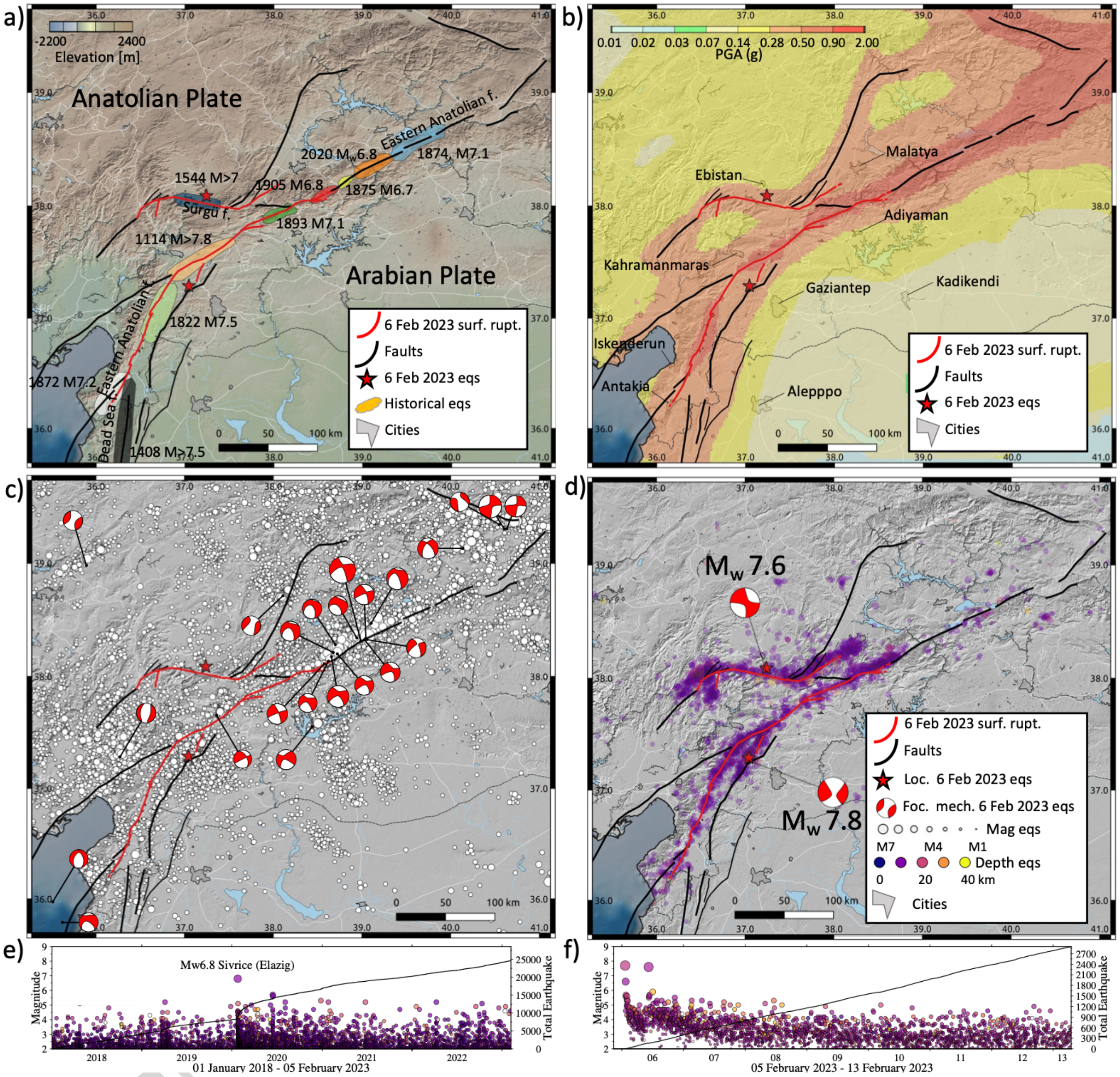

Figure 1. Seismotectonic overview of the East Anatolian Fault region, with the main faults (black lines) and the mapped surface ruptures of the M_w 7.8 and M_w 7.6 earthquakes of February 6, 2023 (red lines). a) Tectonic setting and historical earthquakes (after *Ambraseys, 2009*; *Meghraoui, 2015*). b) Seismic hazard map (peak-ground acceleration (PGA), 10% probability to be exceeded in 50 years) extracted from the Turkish Seismic Hazard Map (by Disaster and Emergency Management Authority, AFAD). c) Background seismicity ($M_w \geq 2$ from AFAD) from January 1, 2018, to February 5, 2023, with focal mechanisms of earthquakes of magnitude $M_w \geq 4.8$ (from global CMT catalog). d) One-week aftershocks ($M_w \geq 2$ from AFAD) and focal mechanism the M_w 7.8 and M_w 7.6 earthquakes of February 6, 2023. e) Time series of background seismicity shown in c). f) Time series of aftershocks shown in d). For details, see Data and Resources.

In the past ~100 years, only a few continental strike-slip earthquakes with magnitudes exceeding M_w 7.5 occurred, limiting the available data and hence detailed studies of such large earthquakes. Examples are the 1990 M_w 7.8 Luzon (Philippines), the 2001 M_w 7.8 Kunlun (China), the 2002 M_w 7.9 Denali (Alaska), the 2013 M_w 7.7 Balouchistan (Pakistan), and the 2016 M_w 7.8 Kaikoura (New Zealand) events. Each of these earthquakes revealed an intricate rupture process related to geometrical fault complexities (*Klinger, 2022 and references therein*): rupture lengths exceeding 100 km and reaching up to 300 km (Kunlun earthquake, 2001); average horizontal surface slip of 3-4 m, reaching locally up to 7-9 m, and strongly varying along-strike in relation to the fault-trace geometry.

The unique character of the 2023 sequence is that two large magnitude earthquakes occurred only 9 hours apart on nearby faults. Pairing of large continental earthquakes over such a short time had not been observed before. Previous pairing always involved longer separation in time, like 14 days between the Tsetserleg (M~8) and Bulnay (M~8) events (*Choi et al., 2018*) and 4 months for the Izmit (M_w 7.4) - Düzce (Mw7.2) sequence (*Konca et al., 2010*). In addition, the spatial dimensions of the two main 2023 quakes, estimated from real-time aftershock locations (Figure 1b) reach lengths of ~350 km on the EAF for the initial M_w 7.8 earthquake and ~170 km for the M_w 7.6 earthquake on the Sürgü Fault. For the regional seismogenic width of 20 km (*Ozer et al, 2019*), these source dimensions are consistent with the events' magnitudes based on source-scaling relations (*Thingbaijam et al, 2017*).

Fault Surface Displacements from Satellite Data

We used pixel-offset tracking of Sentinel-1 radar images to map coseismic surface displacements around the two faults and the extent of surface fault rupturing (*e.g., Fialko et al., 2001; Wang and Jónsson, 2015*). Based on ascending and descending orbit images, as well as along-track (azimuth) and across-track (range) we derived pixel offsets (Figure S1), yielding four different offset images from which we inverted for 3D surface displacements (L*iu et al., 2022*; Figure S2). The resulting horizontal surface displacements and their spatial pattern exhibit left-lateral motion across the two main faults (Figure 2a). Vertical displacements are small in comparison (Figure S2c), confirming the almost pure strike-slip mechanism of both events. The length of the main surface rupture along the EAF in the first earthquake is ~320 km, whereas the surface rupture of the second mainshock is markedly shorter (~150 km). Hence, for both cases the mapped surface rupture is 20-30 km shorter than indicated by aftershock locations (Figure 1d).

Both earthquakes produced large surface-fault offsets (exceedin 4 m) over extended sections along the faults (Figure 2). From their horizontal surface displacement fields, we measured fault offsets at 5 km intervals along the two main faults. The results show that surface fault slip along the EAF has 2-3 slip maxima, with the largest slip found northeast of the epicenter (6-7 m), ~30 km east of the city of Kahramanmaras. Another slip maximum (~4 m) is found further southwest, near Islahiye, with fault slip abruptly decreasing near Antakia at the southwestern end of the rupture. The maximum surface offset of the second fault is even larger than for the first rupture, exceeding 7 m near the epicenter and 6 m over a fault length of ~60 km (Figure 2b). This large surface offset may compensate the relatively short rupture length for the measured magnitude of M_w 7.6.

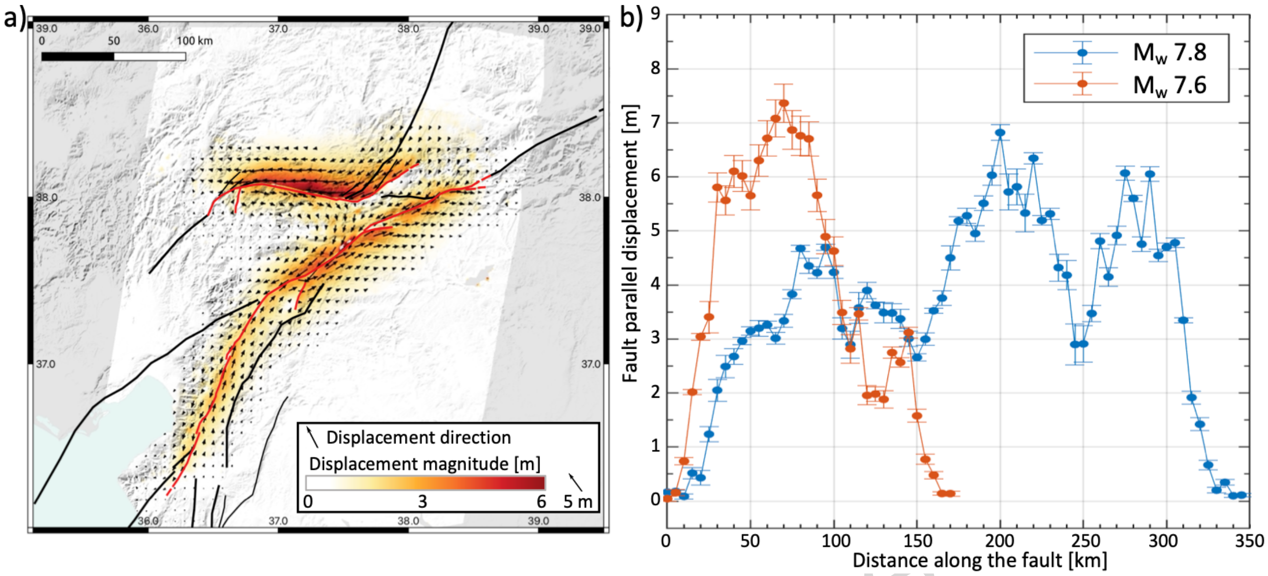

Figure 2. Co-seismic horizontal surface displacements of the Kahramanmaraş earthquakes. a) Map of the amplitude and direction of horizontal displacements derived from pixel-tracking offsets of Sentinel-1 satellite radar images (see text for more details). Red lines show mapped surface ruptures. b) Fault-parallel displacements along the two fault ruptures from southwest to northeast.

Rupture Process from Back-Projection and Finite-Fault Modeling

Using far-field teleseismic data, we estimated the space-time rupture evolution via back-projection (*e.g., Ishii et al., 2005; Koper et al., 2011; Li & Ghosh, 2017*) and finite-fault modeling (*e.g., Mendoza & Hartzell, 2013, and references therein*). For this purpose, we compiled two datasets. For the back-projection, we used seismic stations in Alaska, and selected only stations with average cross-correlation (CC) above 0.6 for the first 25 seconds around the P phase arrival, filtered in the range 0.1 to 2 Hz. This results in 205 and 201 stations for the M_w 7.8 and M_w 7.6 events, respectively. The targeted back-projection region extends from 35° to 39.5°, both in latitude and longitude, with 0.01° grid spacing in both directions. We calculated theoretical travel times based on the PREM model from the source grid to each seismic station, with source depths fixed at catalog depths. In addition, we applied time shifts and relative polarity estimation from the peak CC-coefficients of the first arrival P phases for a shorter 5 s time window, relative to a reference station with maximum average CC-coefficients, as empirical time and polarity correction. To then image the rupture evolution, we deployed a 6-s sliding time window and 0.1-s time step to the continuous waveform data.

Back-projection results show bilateral rupture of the M_w 7.8 earthquake, with an average rupture speed ~2.5 km/s to the east and ~2 km/s to the west, estimated using epicentral distance (which underestimates average rupture velocity along the fault itself if fault geometry changes; Figure S3). However, with a priori knowledge of the fault traces and assuming nearly vertical dip angles, we were able to back-project radiated seismic energy directly to the fault (Figure 3). This better illustrates the complex rupture process of the M_w 7.8 event (inset in Figure 3f). The back-projection suggests bilateral rupture on a small fault east of the EAF, where the hypocenter is located (AFAD catalog). Rupture to the southwest stopped after a few seconds, but continued to the northeast until it reached the intersection with the EAF at ~10 s. The back-projection then locates strong radiation to the east but near the intersection of the nucleation branch and the EAF. This correlates with the strongest recorded ground shaking at station TK4614. The rupture continued to the northeast with an average rupture speed of ~3.1 km/s along the EAF until ~55 s rupture duration, with strong radiation from a short east-west branch of fault, the junction between the EAF and the eastern extension of the Sürgü fault before it stopped ~25 km further east of the junction (Figure 3f inset). The rupture to the southwest along the main EAF appears delayed, with limited seismic radiation west of the epicentral region. However, continued rupture to the east may have altered the stress state on this segment, thereby promoting further rupture to the southwest until ~80 s, when rupture suddenly terminated near Antakya with strong observed seismic radiation.

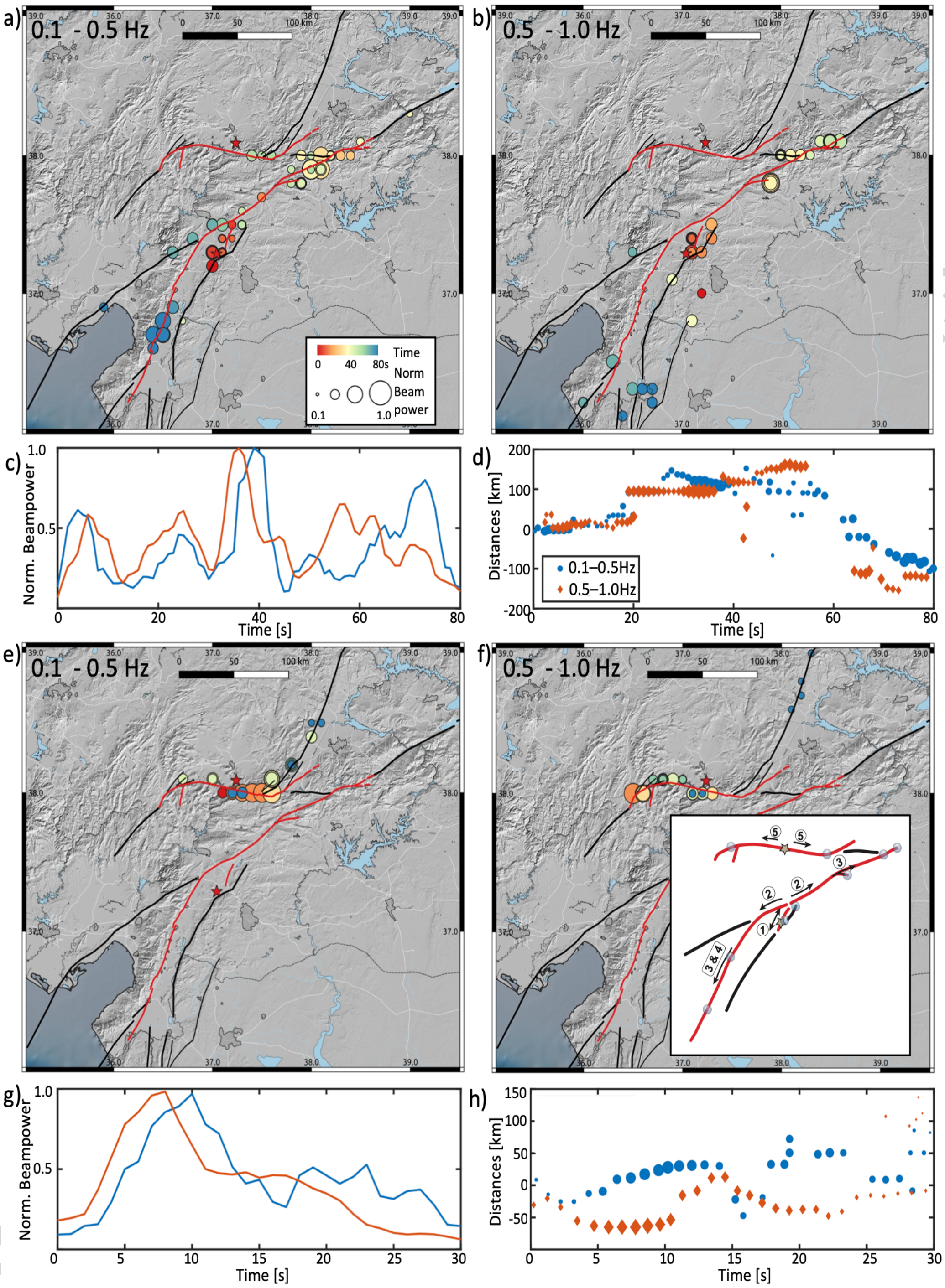

Figure 3. Back-projection results. a) Back-projection results using the Alaska array data filtered in 0.1-0.5 Hz for the M_w 7.8 earthquake. The circles mark the back-projected source locations at the corresponding rupture time. The circle size is proportional to the stacked waveform energy (beampower). b) Same as a) but for frequency range 0.5-1 Hz. c) Normalized beampower evolution with rupture time legend as in d). d) Rupture distance (away from the epicenter) with time. Positive distance indicates rupture to the east of the epicenter, negative distance corresponds to westward rupture. e), f), g) and h) as a), b), c) and d) but for the M_w 7.6 earthquake. In the inset of f), numbered circles depict locations of strong seismic radiation inferred from the back-projection analysis. The arrow indicates the rupture direction, with the associated number representing the rupture sequence.

Back-projection results of the M_w 7.6 event reveal a frequency-dependent rupture process due to rupture directivity (Figure 3e-h, S3) (*Li et al., 2022*). The 0.1-0.5 Hz results capture rupture to the east of the Sürgü Fault, which then changed direction towards the northeast. The 0.5-1 Hz results, on the other hand, mainly track rupture to the west on the Sürgü Fault. Two strong radiation sources are located where fault geometry changes.

In addition to back-projection imaging, we estimated two sets of finite-fault source models for the two earthquakes, one from satellite radar-data derived co-seismic horizontal surface displacements (Figure 2a), the other from teleseismic observations. For the geodetic source model, we used the fault traces mapped from satellite radar offsets, extended the fault lengths a few kilometers beyond the mapped surface ruptures, extended the fault widths to 25 km, and discretized them into 5 km x 5 km fault patches. The first fault is vertical whereas the second mainshock fault dips 78º to the north. We then estimated spatially variable slip on the faults (*e.g., Jónsson et al., 2002*) from the co-seismic horizontal surface displacements, using an appropriate degree of spatial fault slip smoothing.

For inverting teleseismic data to derive kinematic finite-fault source models, we downloaded seismic waveforms for stations situated at teleseismic distances of 30º - 90º, ensuring good azimuthal coverage. By visual inspection, we selected 18 stations for the first mainshock (Figure S4a) and 17 stations for the second event (Figure S5a) with high signal quality, using initially only the P-wave train. Waveforms were then bandpass-filtered (5 – 20 s, Butterworth filter) to remove high-frequency noise. To infer kinematic finite fault parameters, we only used vertical components and applied covariance matrices to account for errors in both measurements and theory (e.g., *Vasyura-Bathke et al., 2020, and references therein*). Because kinematic finite-fault source-parameter estimation suffers from non-unique solutions, we explored the model space using Bayesian inference with Sequential Monte Carlo (SMC) sampling implemented in the BEAT code (*Vasyura-Bathke et al., 2020*) (Figure S4b, S5b).

The kinematic rupture model for the first main event comprises four major segments with uniform dip angle of 89º. Each segment is subdivided into 5 km x 5 km subfaults. Segment 1-a, on which the hypocenter is located, has dimensions of 55 km x 25 km, segment 1-b and 1-c along the EAF expand over 90 km x 25 km, and 80 km x 25 km, respectively, while the southernmost segment 1-d covers an area of 140 km x 25 km (Figure 4). In total, the four fault segments form a 365 km long rupture plane that extends to 25 km depth, parameterized by 365 subfaults.

For the seconds mainshock, we discretized the fault rupture model into three segments each subdivided into 5 km x 5 km subfaults. Segment 2-a, on which rupture nucleated, spans 70 km length; segment 2-b (to the east) and segment 2-c (to the west) are 70 km and 50 km long, respectively (Figure 4a). Each segment extends for 25 km along the fault-dip direction (78° dip angle). The assumed rupture plane is thus 190 km long.

On each subfault, we solved for slip, rupture onset time, and rise time. Furthermore, we allowed for variable rupture velocity, searching in the range of 2.5 - 4.0 km/s. The local source-time function (STF) was set to a half-cosine; the slip direction (rake angle) was allowed to vary in the range -90° to 90° with respect to a reference rake angle of 0° (parallel to the strike direction).

Figure 4 summarizes the finite-fault rupture models inverted from coseismic surface displacements and teleseismic P-wave data. Note that we did not perform any joint inversion, so each model is constrained by a single dataset. However, both models reveal consistent slip distributions. The first M_w 7.8 earthquake is characterized by three main areas of fault slip, showing up to 7 m of slip near the surface on segment 1-b, up to 6 m on segment 1-c, and 4-7 m on segment 1-d (where we find the largest difference between the seismic and the geodetic models). Segment 1-a, on which the rupture started, had less fault slip, but still up to ~3 m (Figure S4c). The southernmost segment 1-d shows an area of high slip before rupture abruptly stops, in agreement with the back-projection results, creating a strong stopping phase. Together with rupture directivity along this 140 km fault segment, strong seismic radiation was generated towards the south, into the Hatay-Antakia region, which, combined with local site effects, created severe local shaking and extensive damage. The total finite-fault seismic moment for this rupture models is 1.03 x 10^{21} Nm (M_w 7.97) and 6.13 x 10^{20} Nm (M_w 7.84) from the teleseismic and geodetic data, respectively.

The back-projection imaging and teleseismic source inversion thus consistently reveal a "T-Bone" geometry with rupture propagating backward relative to the initial direction, seen only in few previous cases, i.e., Kaikoura (*Klinger et al., 2018*), Romanche (*Hicks et al., 2020*) and to a lesser extent Landers event (*Fliss et al., 2005; Wollherr et al, 2019*).

Finite rupture models of the second mainshock show very large near-surface fault slip with maximum slip exceeding 8 m on segment 2-a (on which rupture nucleated, See Figure S5c) along the Sürgü fault, with slip values reaching 6 m over an extended stretch along that segment. Slip values then decreased towards northeast and southwest along segments 2-b and 2-c, respectively. These inferred slip values are in good agreement with surface displacement derived from geodetic data (Figure 2). The inferred seismic moment of this rupture model is 5.03 x 10^{20} (M_w 7.77), and 3.32 x 10^{20} (M_w 7.65) for the seismic and geodetic model, respectively.

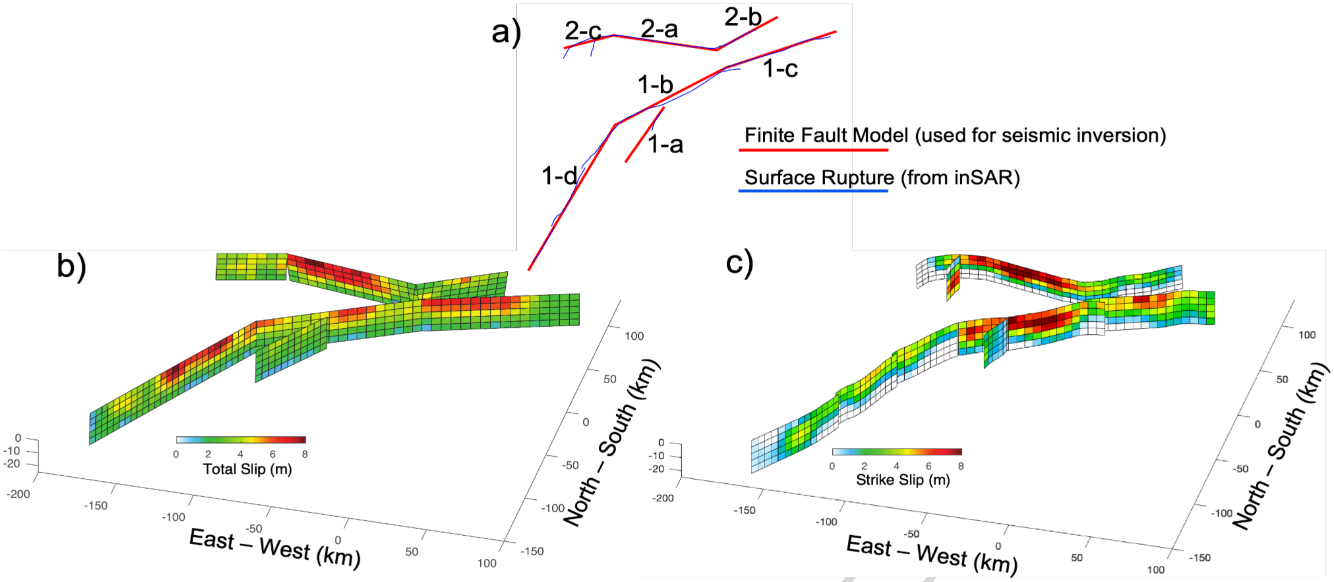

Figure 4. Finite-fault rupture models for the two Kahramanmaraş earthquakes. a) Fault traces used for finite fault inversion (map view), with numbered main segments used in the teleseismic-data inversion. b) Final slip model from teleseismic data, color-coded by total slip magnitude (in meters). The red color saturates at 8 m with the maximum of 8.33 m. c) Final slip model from geodetic data, using the same color-code as in b); the maximum slip value is 8.85 m.

Ground Motion Observations and Shaking Levels

We collected strong motion recordings from the Disaster and Emergency Management Authority (AFAD; see “Data & Resources”) using 254 stations, based on the following selection criteria: (i) instrument response removed, bandpass filter applied (low-cut frequency: 0.025-0.1 Hz, high-cut frequency: 25-40 Hz), and baseline corrected; (ii) no abnormal recordings (e.g., no pre-event signals, no obvious peaks); (iii) three-component recordings available; (iv) VS30 values available. Moreover, we obtained regional-distance seismic waveforms from several sites located along the southward extension of the EAF, the Dead Sea Fault and the Gulf of Aqaba, including stations in Saudi Arabia. We removed the instrument response from waveforms and then filtered them between 0.01 and 50 Hz.

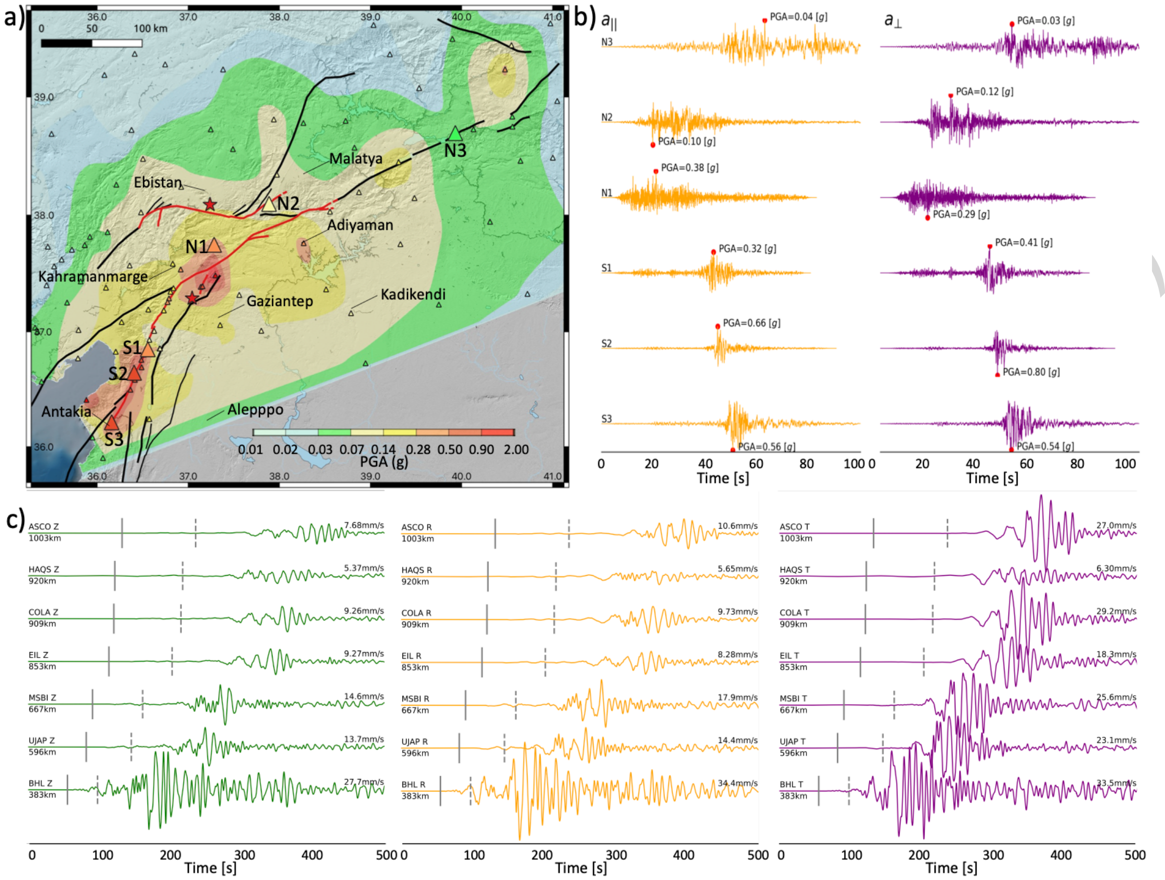

Figure 5. Ground motion observations at local and regional scales for the M_w 7.8 earthquake. a) Spatially interpolated geometric mean of the peak ground acceleration for the fault parallel and normal components. Triangles represent local strong ground motion seismic stations. b) Strong-motion (acceleration) waveforms rotated into fault-parallel (left column) and fault-perpendicular direction with respect to the fault strike (right column). Station symbols S1-S3, and N1-N3 on the map in a) are shown to the left of each waveform. c) Broadband three-component velocity waveforms from stations with azimuth from the source of about 193° (along the Dead Sea Fault). Station names, components and maximum amplitudes are shown to the left of each waveform; epicentral distances are shown on the right-hand side of the waveforms. Vertical lines mark P- and S-arrival times.

Figure 5 presents an overview of locations of strong-motion sites (Figure 5a), selected examples of near-source recordings that illustrate pulse-like motions due to directivity effects and long-duration shaking (Figure 5b), as well as regional-scale waveforms with well-developed surface waves (Figure 5c). The PGA-shakemap in Figure 5a documents peak-ground accelerations exceeding 0.5 g in mainly three areas: near Adiyaman, around the wider epicentral region, and over a large area in the Hatay-Antakia region. Locally, PGA-values reached 1 g, with one site

(TK4614) even showing ~2 g horizontal ground acceleration. In addition, we collected strong motion recordings from 150 stations for the second mainshock, applying the same criteria as for the first event. First order analysis of PGA values of the second event reveals overall lower ground motions (maximum recorded PGA 0.56g at site TK4612, the closest to the epicenter at ~67 km distance) (Figure S12a). However, due to the lack of stations closer to the fault, even higher shaking levels may have occurred but were not recorded.

We further compared observations with two empirical ground-motion models (GMM) used in the 2018 Turkish probabilistic seismic hazard assessment (PSHA) (*Akkar et al., 2018*) (Figures S6 – S11). Whereas the first GMM is specific for Türkiye (*Akkar and Çağnan, 2010*), the second one applies to Europe and the Middle East (*Akkar, et al., 2014)*. Our preliminary analyses suggested that observed ground motions exceed median GMM-predictions for these two GMMs, both for the "raw" observations but also if site-specific corrections for VS30-based site amplification are applied (Figures S7, S9, S11). These observations are consistent with *Gülerce et al. (2016)* who modified the NGA-W1 GMMs using the Turkish strong motion database (so-called "TR-adjusted models"). These TR-adjusted GMMs better replicate the recorded ground motions because they adopted the well-constrained large-magnitude scaling of the global dataset in the NGA-W1 models. Shake-maps for two spectral periods (T = 0.2 s, T = 1.0 s) of pseudo acceleration SA(T) reveal the concentrated strong shaking in several areas (Figure S13 a-d). The regions of particularly high shaking levels correspond approximately to fault areas with high slip, whereby the extended strong shaking in the Hatay-Antakia region can be explained by a combination of strong seismic radiation and local site effects. At several sites (e.g., Antakia, Iskenderun, and Arsuz), the spectral acceleration exceeded the current building code of Türkiye (TBEC-18) at periods T > 1 s that are relevant for tall structures (Figures S13 e-f).

Discussion and Conclusions

We conducted a first-order analysis of the rupture process of the magnitude M_w 7.8 and M_w 7.6 earthquake duplet of February 6, 2023, in south-central Türkiye, using both satellite and seismic data. Both earthquakes are large with predominantly bilateral strike-slip ruptures. The M_w 7.8 earthquake initiated on a side-branch to the EAF and transitioned onto the main EAF with bilateral rupture into the northeast and southwest directions. While the event stopped abruptly in the northeast (after ~55sec), rupture continued to the south where it then terminated after ~80 sec. Directivity effects due to rupture propagation along extended straight fault segments, as well as stopping phases due to sudden rupture cessation at fault extremities led to locally strong seismic radiation for the M_w 7.8 earthquake. The M_w 7.6 earthquake initiated on the Sürgü Fault, 90 km north of the M_w 7.8 epicenter, and ruptured bilaterally for about 150 km. Given its magnitude, the M_w 7.6 rupture is shorter and more compact. Given the length of both ruptures and their strike-slip mechanisms, supershear rupture propagation may locally be expected. We found evidence for such behavior in the back-projection imaging for M_w 7.6 event, but refined analyses based on strong-motion records is needed to confirm this initial observation.

Peak ground accelerations during the M_w 7.8 earthquake locally reached 2 g and exceeded 0.5 g over wide area in the Hatay-Antakia region. Directivity effects and strong stopping phases are partially responsible for the observed strong-motion characteristics. Site effects further amplified ground motions locally. An initial analysis reveals that shaking levels exceeded median predictions from ground-motion models (GMMs) used in the most recent regional PSHA (Figures S6-S11). Locally, observed spectral accelerations exceeded the design spectra of the current building code (Figures S12a and S13). Ground-motions of the 2nd mainshock then hit already weakened or partially collapsed buildings and infrastructure, further increasing damage and destruction. In combination, these effects may provide partial explanations for the wide-spread damage and large destruction of these two earthquakes.

Whilst the occurrence of two such large earthquakes as a “doublet” is uncommon, the second event can be physically explained by stress changes in its epicentral area imposed by the first mainshock that brought the fault closer to failure (*Stein et al., 2023*). Given size and location, we consider the M_w 7.6 earthquake therefore a second mainshock and not an unusually large aftershock. Large strike-slip earthquakes like the M_w 7.8 and 7.6 ruptures of February 6, 2023, are rare, but not uncommon, as they have been observed in the past. Such multi-segment ruptures forming “compounded” events on geometrically complicated fault structures are a challenge in standard probabilistic seismic hazard assessment (PSHA).

Data & Resources

Realtime aftershock locations are provided by the Disaster and Emergency Management Authority (AFAD) (https://deprem.afad.gov.tr/event-catalog; last accessed on February 13, 2023). Focal mechanism solutions of the two mainshocks are from https://geofon.gfz-potsdam.de/old/eqinfo/list.php?mode=mt (last accessed: February 13, 2023). Focal mechanisms of significant seismicity during the period January 1, 2018, to February 6, 2023, can be accessed through https://www.globalcmt.org/. Satellite data are available via the Sentinel data hub https://scihub.copernicus.eu. Teleseimic waveforms for back-projection were downloaded from the Incorporated Research Institutions for Seismology (IRIS) with the link https://ds.iris.edu/wilber3/find_stations/11654089 for the M_w 7.8 event and https://ds.iris.edu/wilber3/find_stations/11654205 for the M_w 7.6 event. Teleseismic waveforms for finite fault inversion were obtained from the Incorporated Research Institutions for Seismology

(IRIS; https://www.iris.edu), Geoforschungsnetz (GEOFON) (https://geofon.gfz-potsdam.de), and Observatories & Research Facilities for European Seismology (ORFEUS; https://www.orfeus-eu.org) data centers, respectively. Broadband waveforms of Figure 5 are from KAUST seismic network (COLA, ASCO, available upon request to the authors), GEOFON (EIL, MSBI, and UJAP, available at https://geofon.gfz-potsdam.de), and Lebanese CNRS (BHL, available upon request to the authors). The strong motion data are available at https://tadas.afad.gov.tr/event-detail/15499 (last accessed February 13, 2023). The 2018 seismic hazard map of Türkiye is available at https://www.resmigazete.gov.tr/eskiler/2018/03/20180318M1-2-1.pdf (last accessed February 13, 2023). High resolution aftershock locations are available from A. Lomax (2023) (*Precise, NLL-SSST-coherence hypocenter catalog for the 2023 Mw 7.8 and Mw 7.6 SE Turkey earthquake sequence. (v2.0) [Data set]. Zenodo. https://doi.org/10.5281/zenodo.7727678).*

Declaration of Competing Interests

The authors declare no competing interest.

Acknowledgements

Geçtiğimiz bu zor günlerde tüm kalbimizle Türkiye ve Suriye vatandaşlarının acılarını paylaşıyoruz. Bu yıkıcı depremlerden etkilenen, ailelerini, arkadaşlarını, komşularını, evlerini ve eşyalarını kaybeden herkese başsağlığı diliyoruz.

قلوبنا متضامنة مع الشعب التركي والسوري في هذه الأوقات العصيبة.

نقدم تعازينا الخالصة لكل من فقد صديق أو قريب أو جار أو منزل أو ممتلكات بسبب الزلازل.

(*We share with all our hearts the suffering of the citizens of Türkiye and Syria during these difficult days. Our condolences to all those affected by these devastating earthquakes, who lost their families, friends, neighbors, homes and belongings*.)

We are indebted to the Saudi Geological Survey (SGS) and the National Center for Geophysics from CNRS of Lebanon for sharing regional-distance seismic waveforms. Comments and constructive criticism by two anonymous reviewers and the Associate Editor helped to improve our work. The research presented in this article is supported by King Abdullah University of Science and Technology (KAUST) in Thuwal, Saudi Arabia, by research grants BAS/1/1339-01-01 and BAS/1/1353-01-01.

References

Akkar, S, Azak, T, Çan, T, Çeken, U, Demircioğlu MB, Duman, T, Erdik, M, Ergintav, S, Kadirioğlu FT, Kalafat, D, Kale, O, Kartal, RF, Kekovali, K, Kilic, T, Özalp, S, Altuncu, S, Şeşetyan, K, Tekin, S, Yakut, A, Yilmaz, MT, Yucemen, MS, Zülfikar, Ö (2018). Evolution of seismic hazard maps in Turkey. Bulletin of Earthquake Engineering, Vol. 16, pp. 3197–3228, doi: 10.1007/s10518-018-0349-1.

Akkar, S, Çağnan, Z (2010). A local ground-motion predictive model for Turkey, and its comparison with other regional and global ground-motion models. Bulletin of the Seismological Society of America, Vol. 100, No. 6, pp. 2978-2995, doi: 10.1785/0120090367.

Akkar, S, Sandıkkaya, MA, Bommer, JJ (2014). Empirical ground-motion models for point- and extended-source crustal earthquake scenarios in Europe and the Middle East. Bulletin of Earthquake Engineering, Vol. 12, pp. 359-387, doi: 10.1007/s10518-013-9461-4.

Aktug, B, Ozener, H, Dogru, A, Sabuncu, A, Turgut, B, Halicioglu, K, Yilmaz, O, Havazli, E (2016). Slip rates and seismic potential on the East Anatolian Fault system using an improved GPS velocity field. Journal of Geodynamics, Vol. 94-95, pp. 1-12, doi: 10.1016/j.jog.2016.01.001.

Ambraseys, N.N. (2009) Earthquakes in the Mediterranean and Middle East: a multidisciplinary study of seismicity up to 1900. Cambridge University Press, Cambridge, MA.

Barka, A. (1996). Slip distribution along the North Anatolian fault associated with the large earthquakes of the period 1939 to 1967. Bulletin of the Seismological Society of America, 86(5), 1238–1254.

Choi J.H., Klinger Y., Ferry M., Ritz J.F., Kurtz R., Rizza M., Bollinger L., Davaasambuu B., Tsend-Ayush N., Demberel S. (2018), Geologic inheritance and earthquake rupture processes: The 1905 $M \geq 8$ Tsetserleg-Bulnay strike-slip earthquake sequence, Mongolia. *J. Geophys. Res., Solid Earth*, **123**, doi : 10.1002/2017JB013962.

Demircioğlu, MB, Şeşetyan, K, Duman, T, Çan, T, Tekin, S, Ergintav, S (2018), Probabilistic seismic hazard assessment for the Turkish territory: part II—fault source and background seismicity model, Bulletin of Earthquake Engineering, Vol. 16, pp. 3399–3438, doi: 10.1007/s10518-017-0130-x.

Fialko, Y., M. Simons, D. Agnew (2001). The complete (3D) surface displacement field in the epicentral area of the 1999 M_w 7.1 Hector Mine earthquake, California, from space geodetic observations, Geophys. Res. Lett., 28, 3063-3066.

Gülerce, Z. , B. Kargıoglu, and N.N. Abrahamson (2016). Turkey-Adjusted NGA-W1 Horizontal Ground Motion Prediction Models, Earthquake Spectra, Volume 32, No. 1, pages 75–100

Hicks, S.P., Okuwaki, R., Steinberg, A., Rychert, C.A., Harmon, N., Abercrombie, R.E., Bogiatzis, P., Schlaphorst, D., Zahradnik, J., Kendall, J- M., Yagi, Y., Shimizu, K., & Sudhaus, H. 2020. Back-propagating supershear rupture in the 2016 Mw 7.1 Romanche transform fault earthquake. Nature Geoscience, 13, 647-653.

Ishii, M., Shearer, P. M., Houston, H., & Vidale, J. E. (2005). Extent, duration and speed of the 2004 Sumatra–Andaman earthquake imaged by the Hi-Net array. *Nature*, *435*(7044), 933-936.

Jónsson, S., H. Zebker, P. Segall & F. Amelung (2002). Fault Slip Distribution of the 1999 Mw7.1 Hector Mine Earthquake, California, estimated from Satellite Radar and GPS Measurements, *Bull. Seismol. Soc. Am.*, 92, 1377-1389.

Klinger Y., Okubo K., Vallage A., Champenois J., Delorme A., Rougier E., Lei. Z., Knight E., Munjiza A., Satriano C., Baize S., Langridge R., Bhat H. (2018). Earthquake damage patterns resolve complex rupture processes. *Geophys. Res. Let.*, 45, doi :10.1029/2018GL078842.

Klinger Y. (2022), Imprint of the continental strike-slip fault geometrical structure in geophysical data, *Geophys. Res. Lett*., 49, e2022GL098146, doi: 10.1029/2022GL098146.

Konca, A. O., Leprince, S., Avouac, J. P., & Helmberger, D. V. (2010). Rupture Process of the 1999 Mw 7.1 Duzce Earthquake from Joint Analysis of SPOT, GPS, InSAR, Strong-Motion, and Teleseismic Data: A Supershear Rupture with Variable Rupture Velocity Rupture Process of the Duzce Earthquake from SPOT, GPS, InSAR, Strong-Motion, and Teleseismic Data. *Bulletin of the Seismological Society of America*, *100*(1), 267-288.

Koper, K.D., A.R. Hutko, T. Lay, C.J. Ammon, H Kanamori (2011), Frequency-dependent rupture process of the 2011 M 9.0 Tohoku Earthquake: Comparison of short-period P wave backprojection images and broadband seismic rupture models, Earth Planets and Space 63 (7), 599

Li, B., & Ghosh, A. (2017). Imaging rupture process of the 2015 Mw 8.3 Illapel earthquake using the US Seismic Array. *The Chile-2015 (Illapel) earthquake and tsunami*, 33-43.

Li, B., Wu, B., Bao, H., Oglesby, D.D., Ghosh, A., Gabriel, A.A., Meng, L. and Chu, R., 2022. Rupture Heterogeneity and Directivity Effects in Back-Projection Analysis. *Journal of Geophysical Research: Solid Earth*, *127*(3), 2021JB022663.

Liu, J., Hu, J., Li, Z., Ma, Z., Shi, J., Xu, W., 2022. Three-Dimensional Surface Displacements of the 8 January 2022 Mw6.7 Menyuan Earthquake, China from Sentinel-1 and ALOS-2 SAR Observations. Remote Sensing, 14(6), 1404, doi: 10.3390/rs14061404.

Meghraoui M. (2015). Paleoseismic history of the Dead Sea Fault Zone. Encyclopedia of earthquake engineering. doi:10.1007/978-3-642-36197-5_40-1.

Mendoza, C. & Hartzell, S. (2013). Finite Fault Source Inversion Using Teleseismic P Waves: Simple Parameterization and Rapid Analysis. Bulletin of the Seismological Society of America, 103 (2A), 834–844. doi: https://doi.org/10.1785/0120120069

Ozer, C., Ozyazicioglu, M., Gok, E. *et al.* (219). Imaging the Crustal Structure Throughout the East Anatolian Fault Zone, Turkey, by Local Earthquake Tomography. *Pure Appl. Geophys.* 176, 2235–2261, https://doi.org/10.1007/s00024-018-2076-6.

Pagani, M, Garcia-Pelaez, J, Gee, R, Johnson, K, Poggi, V, Silva, V, Simionato, M, Danciu, L, Monelli, D, Weatherill, G (2018). The 2018 version of the Global Earthquake Model: Hazard Component. Earthquake Spectra, Vol. 36, No. S1, pp. 226-251. doi: 10.1177/8755293020931866.

Pousse-Beltran, L., Nissen, E., Bergman, E. A., Cambaz, M. D., Gaudreau, É., Karasözen, E., and Tan, F. (2020). The 2020 M_w 6.8 Elazığ (Turkey) earthquake reveals rupture behavior of the East Anatolian Fault. Geophysical Research Letters, 47, e2020GL088136. doi: 10.1029/2020GL088136.

Şeşetyan, K, Demircioğlu, MB, Duman, T, Çan, T, Tekin, S, Eroğlu, Azak T, Zülfikar, Ö (2018). A probabilistic seismic hazard assessment for the Turkish territory part I: the area source model, Bulletin of Earthquake Engineering, Vol. 16, pp. 3367–3397, doi: 10.1007/s10518-016-0005-6.

Stein, R.S.., Toda, S., Özbakir, A. D., Sevilgen, V., Gonzalez-Huizar, H., Lotto, G., Sevilgen, S. 2023, Interactions, stress changes, mysteries, and partial forecasts of the 2023 Kahramanmaraş, Türkiye, earthquakes, Temblor, http://doi.org/10.32858/temblor.299

Thingbaijam, K.K.S., P.M. Mai and K. Goda (2017). New empirical earthquake source scaling laws, Bulletin of the Seismological Society of America, Vol. 107, No. 5, pp. 2225–2246, October 2017, doi: 10.1785/0120170017

Vasyura-Batke, H., J. Dettmer, A. Steinberg, S. Heimann, M. Isken, O. Zielke, S. Jonsson, P.M. Mai, H. Sudhaus (2020) The Bayesian Earthquake Analysis Tool, Seismological Research Letters 91 (2A), 1003-1018.

Wang, T., S. Jónsson, Improved SAR amplitude image offset measurements for deriving three-dimensional coseismic displacements, IEEE Journal of Selected Topics in Applied Earth Obs. & Remote Sensing, doi: 10.1109/JSTARS.2014.2387865, 2015.

Wollherr, S., A.A. Gabriel, P.M. Mai (2019). Landers 1992 "reloaded": Integrative dynamic earthquake rupture modeling. J. Geophys. Res., 124, 6666–6702, doi: 10.1029/2018JB016355